Supplementary information for: Ultrafast electronic line width broadening in the C $1s$ core level of graphene by Davide Curcio et al.

I. EXPERIMENTAL DETAILS

Time- and angle-resolved XPS and valence band photoemission experiments were performed on the PG2 beamline of the FLASH free electron laser (FEL) [1] using hydrogen-intercalated quasi free-standing monolayer graphene on SiC [2, 3] with a hole doping density of $5 \times 10^{12}\,\mathrm{cm}^{-2}$. The sample was annealed in ultra high vacuum (base pressure better than $5 \times 10^{-10}\,\mathrm{mbar}$) at 470 K for 10 min. The sample was held at room temperature during all measurements. Photoelectrons were detected using a momentum microscope covering a momentum range of $6.2\,\mathrm{Å}^{-1}$ with a resolution of $0.06\,\mathrm{Å}^{-1}$ [1]. The analysis of the raw data followed the procedures outlined in Ref. [4] and in Section II. The pump and probe photon energies were 1.55 eV and 337.5 eV (the third harmonic of the FEL), respectively, for the C $1s$ data. The valence band was probed using the first harmonic of the FEL at 112.5 eV. The pump fluence was $\approx 0.5\,\mathrm{mJcm}^{-2}$, and the polarization for both the pump and the probe was linear p-type, with an incidence angle of 68° off-normal, resulting in negligible laser-assisted photoemission replicas with relative intensities of 1.3 % and 2.8 % [5] for the C $1s$ and valence band spectra, respectively. The overall time and energy resolution were 210 fs and 190 meV. Static XPS and XPD data were collected as references at the SuperESCA beamline of Elettra, [6] using the same sample and same excitation photon energy, and with an overall energy and angular resolution of better than 50 meV and ≈ 3°, respectively. The momentum microscope data is known to suffer from space-charge induced energy shifts, especially close to the normal emission axis: These can be corrected based on such reference data [7].

The data shown in Figure 1 of the main text was collected from a k-range of $0.35\,\mathrm{Å}^{-1}$ around the M point of graphene at $\mathbf{k} = (-2.50\ \mathrm{Å}^{-1}, -0.05\ \mathrm{Å}^{-1})$ (location marked in Figure S7), where space-charge effects are minimal due to the distance from normal emission [7].

II. DATA PREPARATION

The raw data obtained for the time-resolved measurements at the PG2 beamline is in the form of tables that require binning into histograms to be visualized and analyzed. The procedure employs the hextof-processor open source code [8] and is outlined elsewhere [1, 4, 9].

In this section, we discuss the calibrations and corrections necessary to convert the binning axes from hardware values (time-of-flight steps, pixels, delay-line position), to physically relevant values (binding energy, k_x and k_y, pump-probe delay t).

The momentum microscope time-of-flight axis is calibrated to binding energy by measuring the C $1s$ spectrum while applying different voltages to the sample that shift the spectrum by a known energy (± 1 eV, 0 eV), and subsequently comparing the resulting C $1s$ spectra to each other and to the ones obtained at the SuperESCA beamline.

The momentum microscope time-of-flight (tof) can be converted to binding energy (E_b) by the following equation:

$$E_b = -\frac{1}{2} m_e \left(\frac{l_0}{tof - tof_0} \right)^2 - W + h\nu + eV_s \quad (1)$$

Where m_e is the rest electron mass, l_0 is the effective microscope drift tube length, tof_0 is the time-of-flight offset, W is the effective work function, $h\nu$ is the photon energy, and V_s is the potential applied to the sample. In particular, note that the conversion is not linear, and the binning needs to be performed directly in binding energy to avoid intensity biases generated by variable bin size across the binning range. The conversion then depends on 3 unknown parameters: tof_0 is found by measuring the so-called "photon peak", which is generated by photons reflected off the sample that cause a count peak on the detector. This is assumed to happen with negligible time-of-flight. Changing l_0 mainly affects the scaling of the binding energy axis, and the parameter can be reliably found by analyzing the voltage-shifted C $1s$ peaks. Finally, W can be found ensuring the resulting C $1s$ peak is found at the same binding energy as the reference spectrum acquired at the SuperESCA beamline.

The binding energy in non-static measurements was found to display a significant **k**-dependent, space-charge induced shift. Pump-induced space-charge has, in fact, the effect of shifting and broadening the spectra with a radial Lorentzian-type dependence [7]. The apparent binding energy shift can be corrected for by following the algorithm presented in Ref. [7], and this was found to significantly improve the quality of the data. While the central position of the correcting Lorentzian, as well as the Lorentzian width parameter, did not vary significantly with pump-probe time delay, the Lorentzian amplitude was found to display a slow, linear dependence on pump-probe delay over the observed time window.

The k_x and k_y axes have been calibrated by matching the position of the dark lines to the photoemission horizons shifted by 2 reciprocal lattice vectors. The photoemission horizon corresponds to a circle with a polar angle of 90°, which is equivalent to a radius of $3.58\,\mathrm{Å}^{-1}$ for the graphene C 1s core level in our measurements.

The optical delay line position is converted to pump-probe delay time t after establishing the pump-probe delay $t = 0$. This has been found by analyzing the time evolution of the integrated intensity in a small energy

range of 200 meV around the graphene C 1s binding energy over acquisition intervals of 400 s. A fit to the data is performed using a double decaying exponential convoluted with a Gaussian, allowing a tracking of any delay drift of the pump or probe over the long acquisition time (22 h). The delay has also been corrected by the bunch arrival monitor values, removing a large part of the probe jitter caused by the self-amplified spontaneous emission process, and improving the time resolution to 210 fs. This can be compared to the time resolution before correction, which was 275 fs.

Gaussian-shaped bins have been employed for the k_x and k_y axes. The Gaussian σ parameters were 0.06 Å^{-1}. The energy and the pump-probe delay axes were binned using rectangular bins with widths of 46 meV and 60 fs, respectively.

The dataset for the pumped sample with no space-charge correction and with rectangular binning for all axes is openly available [10].

III. C 1S SPECTRA

The C 1s spectrum from quasi free-standing monolayer graphene on SiC shows two components, separated by 1.79 eV in binding energy: They are found at 282.59 ± 0.01 eV and at 284.38 ± 0.01 eV. The low binding energy component can be assigned to the carbon atoms in the SiC substrate and the high binding energy component to the graphene layer [11]. The chosen X-ray photon energy renders the experiment very surface-sensitive, suppressing the SiC C 1s peak.

Figure S1 shows the C 1s spectra from the PG2 and SuperESCA beamlines with a binding energy range that allows the small C 1s component from the SiC substrate to be appreciated.

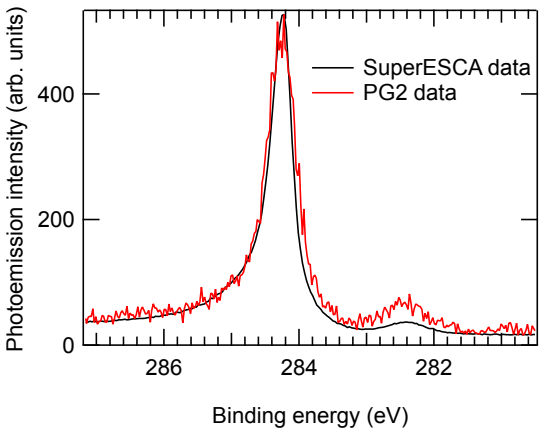

FIG. S1. C 1s spectra acquired at SuperESCA (black line) and at PG2 (red line).

The PG2 spectrum was obtained for negative pump probe delays, in the same k-range as that of Fig. 1 of the main text. The SuperESCA spectrum was obtained close to normal emission. The absolute binding energy was calibrated based on this spectrum combined with a fit of the valence band data using a linear density of states and a Fermi-Dirac distribution. Note that the intensities of the various components in the spectra shown in Fig. S1 are not completely comparable due to the different experimental geometries of the two beamlines.

IV. $D(\epsilon)$ MODELS

An asymmetric XPS line shape for the C 1s core level from weakly doped graphene is commonly observed [2, 12] but not naively expected. After all, the density of states at the Fermi level is approaching zero, leaving only a very small phase space for the inelastic excitations needed to generate a low energy tail in the spectrum. The observed asymmetry has been explained by the fact that in graphene not only electron-hole pair excitations but also plasmon generation can contribute to the asymmetric tail of the C 1s line [13]. Our assumed constant $D(\epsilon)$ and the resulting $J(E')$ for fitting the data using equation (1) in the main text should therefore not be taken as the true density of electronic states in graphene but rather as a phenomenological way of establishing the most simple model for a joint density of possible excitations able to fit the entire data set. In the following we show that a constant $D(\epsilon)$ gives a better fit to the data than a model based the true electronic density of states in graphene.

The most obvious choice for $D(\epsilon)$ would be the density of states of graphene which, for the purpose of the simple illustration here, we approximate by the nearest neighbor tight-binding density of states for the π-band $g(\epsilon)$, with the same amount of hole doping as the quasi free-standing graphene used in the experiment (green line in Figure S2(a)). With this choice for $D(E)$, it is not possible to obtain a satisfactory agreement with the experimental data for any value of the asymmetry parameter a, as demonstrated in Figure S2(b). This is because the experimental data shows a continuous asymmetric tail at higher binding energies, while using $g(\epsilon)$ results in a negligible amount of possible excitations at low energies and a very large number of excitations involving transitions between the van Hove singularities (sharp peaks at roughly 2.9 eV from the Fermi energy). Increasing a does therefore not increase the intensity of the low-energy tail close to the main peak while it creates a pronounced intensity increase at a binding energy 5.8 eV higher than the peak. A different choice for $D(\epsilon)$, namely the constant function $c(\epsilon)$ in Figure S2(a), blue line, gives a much better agreement between model and experiment in Figure S2(b). Indeed, this choice for $D(\epsilon)$ is equivalent to a Doniach-Šunjić function at 0 K, which is a line shape commonly observed to yield good agreement to graphene C 1s spectra [2, 12].

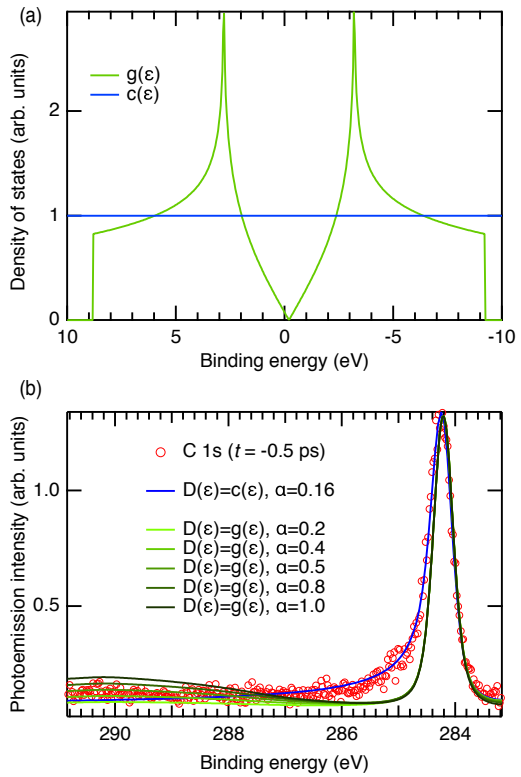

FIG. S2. (a) Different choices for the density of states $D(E)$ near E_F used for fitting the graphene C 1s spectrum. $g(\epsilon)$ is a simple model for graphene (nearest neighbor tight-binding calculation for the π-band. $c(\epsilon)$ is a constant density of states. (b) C 1s spectrum of graphene from PG2 at negative time delay (markers) shown together with line shapes resulting from equation (1) in the main text, using different choices for $D(\epsilon)$ and the asymmetry parameter a.

V. R-FACTOR DEFINITION

The so-called R-factor is a quantity that is used to quantify the agreement between two XPD patterns, $\chi(k_x, k_y)$ and $\chi_0(k_x, k_y)$. The definition is

$$R = \frac{\sum_{k_x,k_y}[\chi(k_x,k_y) - \chi_0(k_x,k_y)]^2}{\sum_{k_x,k_y}\chi(k_x,k_y)^2 + \chi_0(k_x,k_y)^2}, \qquad (2)$$

where typically $\chi(k_x, k_y)$ is an experimental modulation function while $\chi_0(k_x, k_y)$ is a simulated modulation function [14]. Modulation functions are introduced as

$$\chi(k_x,k_y) = \frac{I(k_x,k_y) - I_0(k_x,k_y)}{I_0(k_x,k_y)} \qquad (3)$$

where $I(k_x, k_y)$ is an intensity distribution, and $I_0(k_x, k_y)$ is a smooth function approximating the photoemission intensity in the absence of any scatterers. The modulation function then represents the photoemission intensity variations that are due to diffraction.

VI. MULTIPLE SCATTERING SIMULATIONS

In order to evaluate the effect of inelastic electron-hole pair generation/annihilation during the photoemission process on the XPD pattern by simulations (see Section VII), it is desirable to obtain a realistic description of the observed diffraction pattern. To do so, we have performed simulations of XPD patterns using the EDAC code [15]. This code can perform multiple scattering simulations of electrons in atomic clusters, and we compared the results to the XPD patterns obtained at the SuperESCA beamline. The SuperESCA data (see Fig. S1) have the advantage of a much higher signal to noise ratio compared to the PG2 data. Note that while the same photon energy was used at SuperESCA and PG2, the resulting XPD patterns are not expected to be identical due to differences in experimental geometry/light polarization at the two sources.

Using the known structural parameters of graphene, optimized values for V_0 (muffin tin inner potential), λ_i (inelastic mean free path), R_{max} (radius of the atomic cluster), l_{max} (maximum angular momentum quantum number used in the calculation), and number of scattering orders, have been found by direct comparison with the SuperESCA experimental XPD pattern, as well as by convergence tests for the calculation. The optimization of V_0 and λ_i has been accomplished by minimizing the R-factor, calculated by excluding the area affected by the dark lines, since they are not captured by our multiple scattering simulations that use an abrupt step in the muffin tin surface potential. Multiple scattering simulations using the parameters found here can then be used to simulate XPD patterns in the different experimental geometry of the PG2 beamline.

Fig. S3 shows the resulting comparison between the experimental pattern and the optimized multiple scattering simulation, obtained with the following simulation parameters: $V_0 = 17.2\,\text{eV}$, $\lambda_i = 5\,\text{Å}$, $l_{max} = 8$, $R_{max} = 15\,\text{Å}$, number of scattering orders = 17. The kinetic energy was set at 49.1 eV, which is the kinetic energy measured by the electron analyzer for the graphene C 1s component. The simulated structure only includes the graphene layer, with no substrate, since the lattices have a different unit cell, and the effect of the substrate would thus be averaged out in a local cluster calculation. Neglecting the substrate is known to be an excellent approximation [12].

VII. EFFECT OF INELASTIC ELECTRON-HOLE PAIR GENERATION/ANNIHILATION ON R(T)

Being able to simulate XPD patterns, we can evaluate the effect of core electron deflection by inelastic electron-hole generation/annihilation at high electronic temperatures. Specifically, we can test if such effects would be consistent with the very small change of $R(t)$ shown in

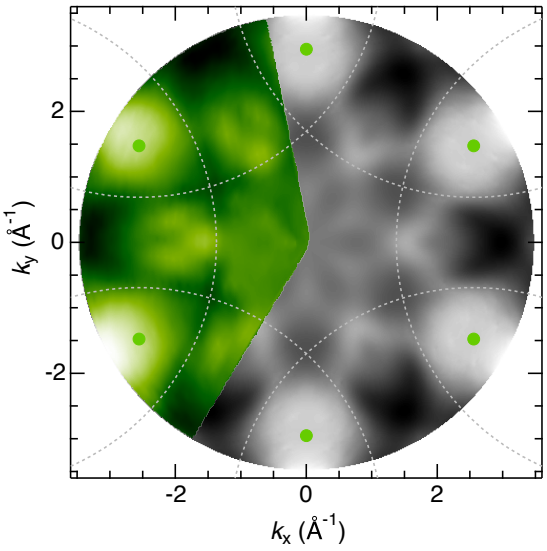

FIG. S3. Analysis of the XPD data collected at the SuperESCA beamline. Experimental (green) and simulated (gray) XPD pattern for the graphene C 1s component at $h\nu$ =337.5 eV. The gray dashed lines are the photoemission horizon location (polar angle $\theta = 90°$) shifted by 2 BZs. Γ points are indicated by green markers.

Fig. 3(d) of the main text. We have argued that, at high electronic temperature, the C 1s photoelectrons have a high probability of leaving the solid with one or several electron-hole pairs created or annihilated. The energy loss (gain) is accompanied by a momentum change that, due to the strong constraints by the electronic structure of graphene is either nearly zero or $K - K'$ for intravalley and intervalley excitations, respectively (modulo a reciprocal lattice vector). We can now simulate how the presence of such excitations would affect the XPD pattern.

The excitation (annihilation) of electron-hole pairs is part of the photoemission process and can be considered to be instantaneous for our purposes. We thus have to simulate the situation of a photoelectron escaping that is deflected by a reciprocal lattice vector, by $K - K'$ (or the identical vector $\Gamma - K$) or by a combination of both. We use the following way to implement this in the multiple scattering simulation: Since the initial state for C 1s has angular momentum $l = 0$, due to the photoemission selection rules, the final state angular momentum quantum number is $l = 1$. Therefore the directionality of the final state is determined by a single vector, the electric field direction of the probe pulse. Deflecting the momentum of the photoelectron can thus be implemented by changing the electric field direction in the multiple scattering simulations accordingly. The contribution of such deflected photoelectrons to the XPD pattern can then be estimated by summing the photoemission intensity from photoelectrons deflected by $\Gamma - K$ or a reciprocal lattice vector and those without a momentum change.

In Fig. S4 the resulting modulation functions are shown. Panel (a) displays the simulated pattern in the PG2 experimental conditions without the inclusion of inelastically deflected photoelectrons. Note that this XPD pattern is slightly different from that in Fig. S1 due to the fact the impinging photon beam axis has a fixed angle with respect to the surface of the sample, reducing the symmetry of the pattern. Note also that the pattern is quite similar to the experimental pattern from PG2 as shown in Fig. 3(a) of the main text, with both showing an intensity depletion around Γ_1 and a minimum in the azimuthal modulation around the M points at the edges of the observed pattern.

Fig. S4(b) and (c) show the XPD pattern with a substantial contribution of inelastically deflected photoelectrons. The deflection is included either only by the sum of six equivalent $\Gamma_1 - \Gamma_2$ reciprocal lattice vectors or by these and the six equivalent $\Gamma_1 - K$ vectors. We shall see in Section VIII that such an admixture of inelastically scattered intensity is sufficient to cause the observed reduction of the C 1s binding energy variation $\Delta(\Gamma_1, \Gamma_2)$.

The change of the XPD patterns upon mixing deflected photoelectrons can be tracked by an R-factor defined the same way as $R(t)$. The corresponding values are given in the figure. Interestingly, even substantial inelastic contributions only lead to a small change of the XPD pattern with R values that are comparable to the maximum $R(t)$ in Fig. 3(d). As pointed out in connection with Fig. 3, the main reason for this is that the direction of the primary photoelectron wave in the XPD process mainly influences the intensity of the diffraction features and not so much their locations which, in turn, are governed by the atomic structure.

We stress that the dark lines have been added artificially in Fig. S4, by multiplying the modulation function of the pattern by a value smaller than 1 with a Gaussian profile as a function of distance from the dark line. This has been done to give a better estimate of the R-factor increase.

VIII. QUANTITATIVE THEORETICAL ESTIMATION OF $\Delta(\Gamma_1, \Gamma_2)$

As for the XPD pattern, we can simulate the effect of some photoelectrons being deflected by a reciprocal lattice vector or by $K - K'$ (i.e. $\Gamma - K$) on $\Delta(\Gamma_1, \Gamma_2)$, the observed energy difference between the Γ_1 and Γ_2 points. We first simulate how the C 1s dispersion is expected to be observed as a **k**-dependent shift of the core level binding energy. The C 1s dispersion is shown in Fig. S5(a). The expected photoemission intensity due to the sublattice interference in the bipartite lattice is encoded in the grayscale of the plotted dispersion. Using this dispersion as a starting point, a simulated C 1s spectrum is generated for each **k** point by summing two Doniach-Šunjić functions with line shape parameters that are given by fitting the experimental spectra. The peak energies are

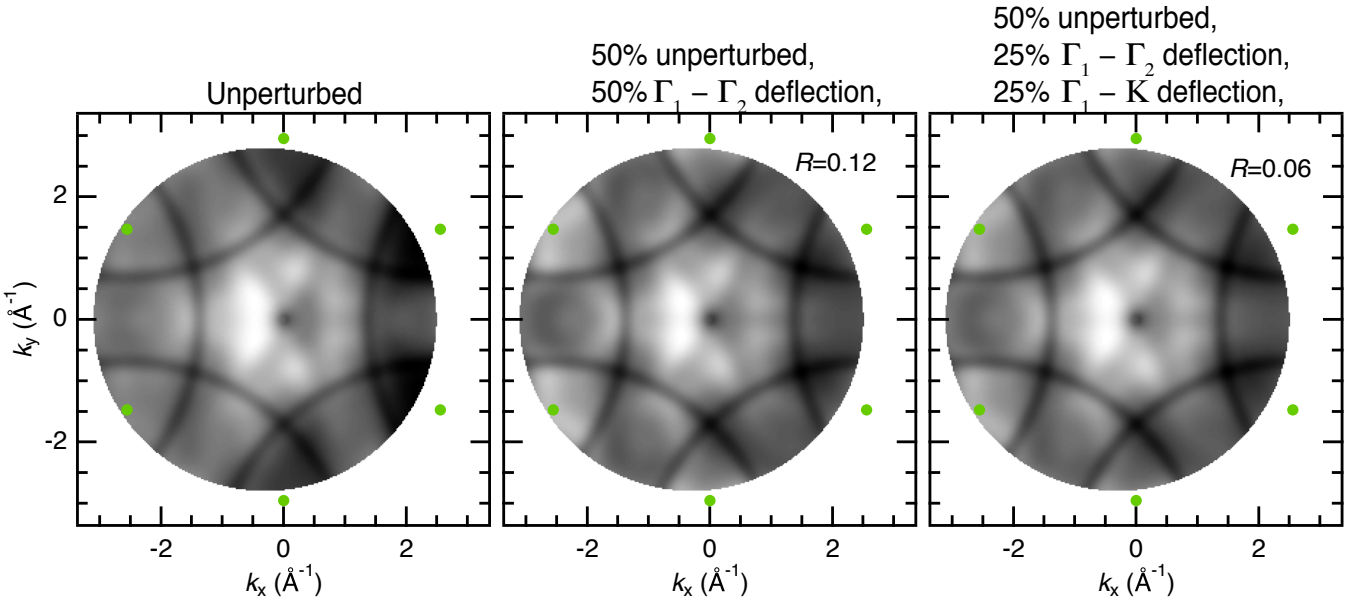

FIG. S4. Multiple scattering simulations for the C 1*s* XPD pattern from the PG2 beamline at FLASH. The simulation parameters are the same as what has been found to optimize agreement with the SuperESCA experimental data in Fig. S4. The simulated experimental geometry, however, is the same as PG2 geometry. Patterns are displayed with artificially added dark lines.

taken from the tight-binding model in Fig. S5(a), i.e., from a σ-band with a bonding anti-bonding splitting of 60 meV. The peak intensities are calculated based on the expected sub-lattice interference [12]. While each spectrum is then the sum of two C 1*s* peaks, these individual contributions cannot be resolved because their separation is much smaller than the width of each peak. In fact, the entire spectrum can be well-approximated by a single Doniach-Šunjić function. The binding energy resulting from fitting a single Doniach-Šunjić function to the synthetic data is plotted in Fig. S5(b). The *observed* bonding anti-bonding splitting, i.e., $\Delta(\Gamma_1, \Gamma_2)$, is 45 meV and not 60 meV. This is caused by the incomplete suppression of the bonding band close to Γ_2 which is in contrast to the complete extinction of the anti-bonding band at Γ_1 (see Fig. S5(a)).

To investigate the change of $\Delta(\Gamma_1, \Gamma_2)$ as a result of inelastic electron deflection, we create the same artificial C 1*s* spectra as described before but add additional spectra that have been shifted by some **k** vector before performing the analysis leading to the **k**-resolved apparent binding energy shown in Fig. S5. The results are summarized in Fig. S6. We consider momentum deflections corresponding to $\Gamma_1 - K$ for the six closest K-points, as well as $\Gamma_1 - \Gamma_2$ deflections for the six closest reciprocal lattice vectors. We study how mixing these into the photoemission intensity would affect $\Delta(\Gamma_1, \Gamma_2)$. In order to observe a change of $\Delta(\Gamma_1, \Gamma_2)$ from 45 meV to 10 meV, 60 % of the observed signal needs to have inelastic origin in the case that both $\Gamma_1 - \Gamma_2$ and $\Gamma_1 - K$ deflection is taken into account, or 50 % of the observed signal needs to have been deflected in the case that only $\Gamma_1 - \Gamma_2$ deflection is taken into account. Such relatively high inelastic contributions appear plausible in view of the substantial line broadening at the highest electronic temperatures in Fig. 1 and we stress again that this scenario would not be inconsistent with the only minor change of the XPD pattern in Fig. 3.

IX. C 1*s* BINDING ENERGY AT THE M POINTS

In order to verify that the observed C 1*s* binding energy difference $\Delta(\Gamma_1, \Gamma_2)$ is not an experimental artefact, the C 1*s* band was also measured at non-equivalent M points placed at different distances from the normal emission axis (see inset in Fig. S7). In the area visible on the detector, it is possible to find six M_1 points between the first BZ and neighboring zones (downward pointing blue triangles in Fig. S7), and three M_2 points further away from normal emission (upward pointing purple triangles in Fig. S7).

The time-resolved binding energy difference $\Delta(M_1, M_2)$ for the average of the two inequivalent M point families is shown in Fig. S7. The binding energy difference shows an unequivocally reduced change compared to $\Delta(\Gamma_1, \Gamma_2)$ (or none at all), confirming the reciprocal-lattice-aware origin for the C 1*s* binding energy. Note that the theoretical difference in observed binding energy for the different types of M points used here is 15 meV, and not strictly 0 meV. This is again

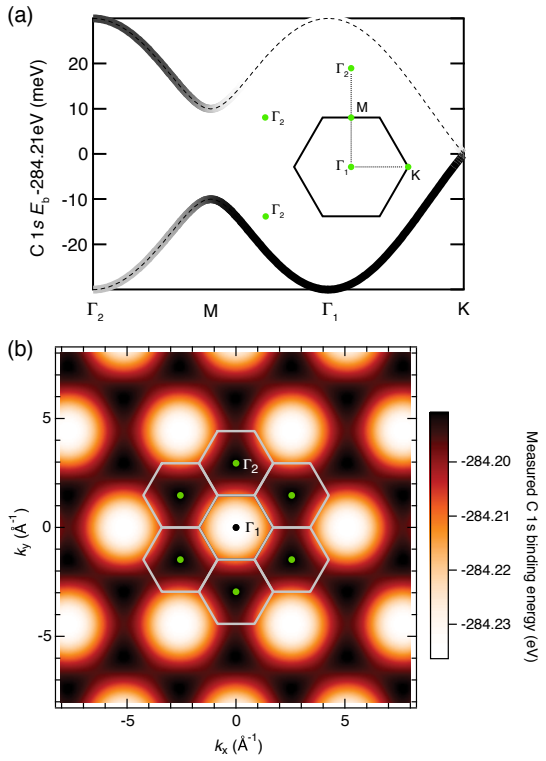

FIG. S5. (a) Tight-binding band structure of the C 1s core level states along the dotted line in the inset. The dashed lines show the dispersion of the bonding and anti-bonding bands. The grayscale shading encodes the expected photoemission intensity due to the sub-lattice interference effects. Dark corresponds to high intensity. (b) Map of the expected **k**-dependent C 1s binding energy for simulated data. The reciprocal lattice and the position of the Γ points are indicated. Note that, due to the sub-lattice interference effect, the observed periodicity of the C 1s binding energy modulation is twice as large as the reciprocal lattice.

caused by the different photoemission intensities of the bonding and anti-bonding bands, caused by the selection rules of the bipartite lattice.

X. FROZEN PHONON BAND STRUCTURE

Almost immediately after the electronic excitation, energy is transferred to the strongly coupled $E_{2g}(LO)$ and $A_1'(TO)$ optical phonon modes in the vicinity of the Γ and K points, respectively [16], increasing their temperature T_p (see Figure 2 of the main text). Given the high energies of these modes, a temperature of around $T_p \approx 3000\,\mathrm{K}$ is reached without a significant increase in population. Nevertheless, we explore the effect of such excited lattice vibrations on the core level dispersion, considering it as a possible cause of the line width increase and the ultrafast change of $\Delta(\Gamma_1, \Gamma_2)$. For this purpose, we adopt the so-called "frozen phonon" approach. Specifically, we

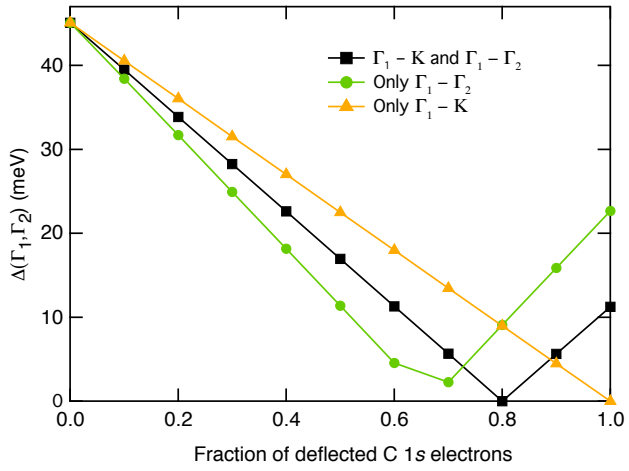

FIG. S6. Observed C 1s band width, expressed in terms of $\Delta(\Gamma_1, \Gamma_2)$, for simulated data when considering deflections of the outgoing core electrons by different momentum changes.

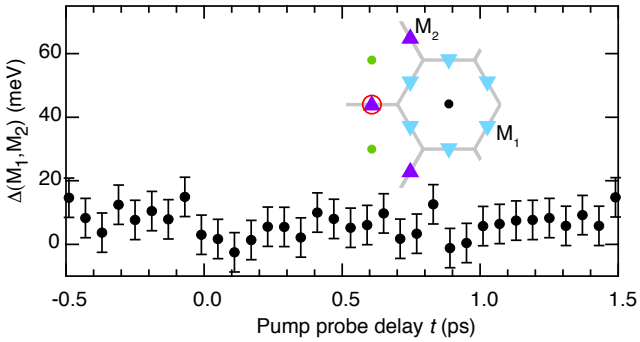

FIG. S7. Binding energy changes measured at M points in the first and neighboring Brillouin zones. The vertical energy scale corresponds to that shown in Fig. 4. In the inset, BZ boundaries are displayed in gray, Γ points are displayed as circles (black in the first BZ, green in the neighboring BZs), first BZ M points (M_1) as downward pointing blue triangles, neighboring BZ M points (M_2) as upwards pointing purple triangles. The red circle around the leftmost M point marks the area used for the analysis presented in Fig. 1 of the main paper.

calculate the C 1s bands for 1 pm atomic displacements corresponding to the lattice deformations due to $E_{2g}(LO)$ and $A_1'(TO)$ phonon modes.

The C 1s dispersions were obtained by all-electron Density Functional Theory (DFT) calculations using the Perdew-Burke-Ernzerhof exchange-correlation functional, as implemented in the code CRYSTAL14 [17–19]. An atomic natural orbital Gaussian basis set has been used and our calculations were done using a 16×16 (8×8) Monkhorst-Pack k-grid for the $E_{2g}(LO)$ ($A_1'(TO)$) phonon, respectively. For convergence, we applied a Fock

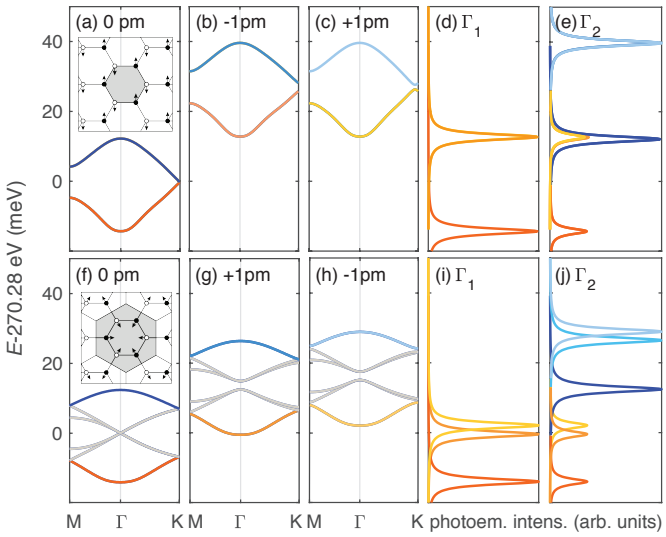

FIG. S8. (a)-(c) Graphene 1s DFT band structures corresponding to the $E_{2g}(LO)$ phonon mode at the equilibrium (a), and for atomic displacements of 1 pm (b) and −1 pm (c), in the directions indicated by the arrows in the inset of panel (a). (d),(e) Photoemission intensity at Γ_1 and Γ_2, respectively, estimated from a tight-binding model as explained in the text. The colors correspond to photoemission from the bands in (a)-(c). (f)-(h) Graphene 1s DFT band structures corresponding to the $A_1'(TO)$ mode, folded within the supercell represented in the inset of panel (f), at the equilibrium (f) and for atomic displacements of 1pm (g) and 1 −pm (h), in the directions indicated in the inset of panel (f). (i),(j) Photoemission intensity at Γ_1 and Γ_2, estimated from a tight-binding model. The symmetry points, K and M, refer to the primitive and supercell (reduced) BZ in panels (a)-(c) and (f)-(h), respectively. All energies are given with respect to the vacuum level.

(Kohn-Sham) matrix mixing of 97% between subsequent self-consistent field cycles and the convergence on total energy was set to 10^{-8} Hartrees.

In order to evaluate the effect of the band structure distortions on the C 1s spectra at Γ_1 and Γ_2, we have employed a tight-binding model and followed the procedure of Ref. 20 to calculate the modulus-squares of the Bloch-states' Fourier components at Γ_1 and Γ_2 —which are directly related to the photoemission intensities [21, 22]. The tight-binding parameters where obtained from the DFT band structures. In order to incorporate the lattice deformations, we assumed that the hopping between the s-orbitals decreases exponentially as a function of the atomic distances. Our model consists of three parameters: the hopping between s-orbitals at the equilibrium distance, the exponential decay rate and the on-site energy (i.e., the energy distance with respect to the vacuum level). Note that the relative photoemission intensities between Γ_1 and Γ_2 are not directly comparable.

The effect of a static lattice distortion following the displacement pattern of the $E_{2g}(LO)$ mode at Γ is shown in Figure S8(b) and (c), starting from the equilibrium dispersion in Figure S8(a). Displacements of ± 1 pm are applied along the arrows in the inset of Figure S8(a). The lattice distortion results in a small overall shift of the band structure to lower binding energy and hardly any effect on $\Delta(\Gamma_1, \Gamma_2)$. A noticeable effect on the $\Delta(\Gamma_1, \Gamma_2)$ can only be obtained by going to larger displacements but these can be ruled out because they would result in an *increase* of $\Delta(\Gamma_1, \Gamma_2)$ —which is opposite to the observed behavior. Moreover, larger displacements would induce major changes of the band structure near the Fermi level (not shown), which are not observed experimentally [23–27]. Figure S8(d) and (e) show the simulated photoemission spectra at Γ_1 and Γ_2. Each panel shows the photoemission intensity for the equilibrium structure and the two distorted structures, such that the peak colors corresponds to the band colors in Figure S8(a)-(c). In the first BZ zone, at Γ_1, photoemission from the anti-bonding bands is completely suppressed whereas near Γ_2 the bonding bands still have some spectral weight. As expected from the band structure calculations, the core levels spectra merely show a small shift.

Fig. S8(f)-(j) shows the corresponding results for the A_1' phonon at K. In contrast to the E_{2g} mode, the static lattice distortion results in a larger unit cell in real space and, therefore, a smaller BZ (see the unit cell indicated in gray in Figure S8(f)). The DFT band structures are shown within this supercell BZ. The smaller size of the BZ causes a back-folding of the band structure from the original BZ and the resulting new bands at Γ are shown in gray. In principle, these bands could be relevant for both the broadening of the C 1s peak and the reduction of $\Delta(\Gamma_1, \Gamma_2)$. In order to simulate the photoemission intensities at Γ_1 and Γ_2, we used our tight-binding model for the supercell shown in the inset of Fig. S8(f), adapated the tight-binding bands to be similar to the DFT bands in Figure S8(f)-(h) and then unfolded those bands into the BZ of undeformed graphene. The resulting intensities are shown in Figure S8(i) and (j). As a result of the photoemission matrix elements (essentially due to the same sub-lattice interference effects that suppress the bonding band at Γ_2 [21, 22]), the intensity from the gray back-folded bands is very small compared to the other bands. The presence of these bands can thus not explain the observed reduction of $\Delta(\Gamma_1, \Gamma_2)$ or the broadening of the peak. We also note that, as for the E_{2g} mode, larger unphysical static distortions would lead to an apparent increase of $\Delta(\Gamma_1, \Gamma_2)$, rather than to the observed decrease.

Overall, our calculations suggest that neither the broadening nor the $\Delta(\Gamma_1, \Gamma_2)$ reduction can be explained in terms of a band structure change caused by the excitation of the $E_{2g}(LO)$ and $A_1'(TO)$ optical phonons.

XI. GW CORRECTED BAND STRUCTURE

In principle, the ultrafast reduction of $\Delta(\Gamma_1, \Gamma_2)$ may be caused by temperature-dependent effects on the elec-

tronic structure. In order to exclude this, we have performed finite-temperature GW calculations of the C 1s band structure. For this purpose we calculated the electronic structure using the FlapwMBPT software package [28] with the generalized gradient approximation as parameterized in Perdew-Burke-Ernzerhof [29]. We employed an all-electron basis set and a $21\times21\times2$ k-grid. 15 steps of quasi-self consistent GW were sufficient to converge $\Delta(\Gamma_1,\Gamma_2)$ to better than 1.0 meV. Interestingly, at zero-temperature we find that $\Delta_{T=0}(\Gamma_1,\Gamma_2)$ =46 meV —which is in better agreement with the experimental result than the previously reported DFT value of 25 meV [12]. However, no appreciable temperature dependence of the band structure is observed. In fact, we also find $\Delta_{T=3500\mathrm{K}}(\Gamma_1,\Gamma_2)$ = 46 meV. This suggests that the time-dependent variation of the C 1s line shape cannot be ascribed to a temperature dependence of electronic many-body effects.

[1] D. Kutnyakhov, R. P. Xian, M. Dendzik, M. Heber, F. Pressacco, S. Y. Agustsson, L. Wenthaus, H. Meyer, S. Gieschen, G. Mercurio, A. Benz, K. Bühlman, S. Däster, R. Gort, D. Curcio, K. Volckaert, M. Bianchi, C. Sanders, J. A. Miwa, S. Ulstrup, A. Oelsner, C. Tusche, Y.-J. Chen, D. Vasilyev, K. Medjanik, G. Brenner, S. Dziarzhytski, H. Redlin, B. Manschwetus, S. Dong, J. Hauer, L. Rettig, F. Diekmann, K. Rossnagel, J. Demsar, H.-J. Elmers, P. Hofmann, R. Ernstorfer, G. Schönhense, Y. Acremann, and W. Wurth, Time- and momentum-resolved photoemission studies using time-of-flight momentum microscopy at a free-electron laser, Review of Scientific Instruments **91**, 013109 (2020).

[2] C. Riedl, C. Coletti, T. Iwasaki, A. A. Zakharov, and U. Starke, Quasi-free-standing epitaxial graphene on SiC obtained by hydrogen intercalation, Physical Review Letters **103**, 246804 (2009).

[3] F. Speck, J. Jobst, F. Fromm, M. Ostler, D. Waldmann, M. Hundhausen, H. B. Weber, and T. Seyller, The quasi-free-standing nature of graphene on H-saturated SiC(0001), Applied Physics Letters **99**, 122106 (2011).

[4] R. P. Xian, Y. Acremann, S. Y. Agustsson, M. Dendzik, K. Bühlmann, D. Curcio, D. Kutnyakhov, F. Pressacco, M. Heber, S. Dong, T. Pincelli, J. Demsar, W. Wurth, P. Hofmann, M. Wolf, M. Scheidgen, L. Rettig, and R. Ernstorfer, An open-source, end-to-end workflow for multidimensional photoemission spectroscopy, Scientific Data **7**, 442 (2020).

[5] M. Keunecke, M. Reutzel, D. Schmitt, A. Osterkorn, T. A. Mishra, C. Möller, W. Bennecke, G. S. M. Jansen, D. Steil, S. R. Manmana, S. Steil, S. Kehrein, and S. Mathias, Electromagnetic dressing of the electron energy spectrum of Au(111) at high momenta, Phys. Rev. B **102**, 161403 (2020).

[6] A. Abrami, M. Barnaba, L. Battistello, A. Bianco, B. Brena, G. Cautero, H. Chen, Q, D. Cocco, G. Comelli, S. Contrino, F. DeBona, S. Di Fonzo, C. Fava, P. Finetti, P. Furlan, A. Galimberti, A. Gambitta, D. Giuressi, R. Godnig, W. Jark, S. Lizzit, F. Mazzolini, P. Melpignano, L. Olivi, G. Paolucci, R. Pugliese, S. N. Qian, R. Rosei, G. Sandrin, A. Savoia, R. Sergo, G. Sostero, R. Tommasini, M. Tudor, D. Vivoda, F.-Q. Wei, and F. Zanini, Super ESCA: First beamline operating at ELETTRA, Review of Scientific Instruments **66**, 1618 (1995).

[7] B. Schönhense, K. Medjanik, O. Fedchenko, S. Chernov, M. Ellguth, D. Vasilyev, A. Oelsner, J. Viefhaus, D. Kutnyakhov, W. Wurth, H. J. Elmers, and G. Schönhense, Multidimensional photoemission spectroscopy—the space-charge limit, New Journal of Physics **20**, 033004 (2018).

[8] S. Y. Agustsson, D. Curcio, R. P. Xian, M. Z. Sohail, M. Heber, M. Scholz, and Y. Acremann, momentoscope/hextof-processor:hextofprocessor-v1.0.4 (2021).

[9] M. Dendzik, R. P. Xian, E. Perfetto, D. Sangalli, D. Kutnyakhov, S. Dong, S. Beaulieu, T. Pincelli, F. Pressacco, D. Curcio, S. Y. Agustsson, M. Heber, J. Hauer, W. Wurth, G. Brenner, Y. Acremann, P. Hofmann, M. Wolf, A. Marini, G. Stefanucci, L. Rettig, and R. Ernstorfer, Observation of an excitonic Mott transition through ultrafast core-cum-conduction photoemission spectroscopy, Phys. Rev. Lett. **125**, 096401 (2020).

[10] D. Curcio, S. Pakdel, K. Volckaert, J. A. Miwa, S. Ulstrup, N. Lanatà, M. Bianchi, D. Kutnyakhov, F. Pressacco, G. Brenner, S. Dziarzhytski, H. Redlin, S. Agustsson, K. Medjanik, D. Vasilyev, H.-J. Elmers, G. Schönhense, C. Tusche, Y.-J. Chen, F. Speck, T. Seyller, K. Bühlmann, R. Gort, F. Diekmann, K. Rossnagel, Y. Acremann, J. Demsar, W. Wurth, D. Lizzit, L. Bignardi, P. Lacovig, S. Lizzit, C. E. Sanders, and P. Hofmann, Ultrafast electronic line width broadening in the C 1s core level of graphene, 10.5281/zenodo.4773850 (2021).

[11] C. Coletti, K. V. Emtsev, A. A. Zakharov, T. Ouisse, D. Chaussende, and U. Starke, Large area quasi-free standing monolayer graphene on 3c-SiC(111), Applied Physics Letters **99**, 081904 (2011).

[12] S. Lizzit, G. Zampieri, L. Petaccia, R. Larciprete, P. Lacovig, E. D. L. Rienks, G. Bihlmayer, A. Baraldi, and P. Hofmann, Band dispersion in the deep C 1s core level of graphene, Nature Physics **6**, 345 (2010).

[13] B. E. Sernelius, Core-level spectra from graphene, Phys. Rev. B **91**, 045402 (2015).

[14] D. P. Woodruff and A. M. Bradshaw, Adsorbate structure determination on surfaces using photoelectron diffraction, Reports on Progress in Physics **57**, 1029 (1994).

[15] F. J. García de Abajo, M. A. Van Hove, and C. S. Fadley, Multiple scattering of electrons in solids and molecules: A cluster-model approach, Phys. Rev. B **63**, 075404 (2001).

[16] F. Caruso, D. Novko, and C. Draxl, Photoemission signatures of nonequilibrium carrier dynamics from first principles, Phys. Rev. B **101**, 035128 (2020).

[17] R. Dovesi, R. Orlando, A. Erba, C. M. Zicovich-Wilson, B. Civalleri, S. Casassa, L. Maschio, M. Ferrabone, M. De La Pierre, P. D'Arco, *et al.*, Crystal14: A program for the ab initio investigation of crystalline solids, Int. J. Quantum Chem. **114**, 1287 (2014).

[18] R. Dovesi, V. Saunders, C. Roetti, R. Orlando, C. Zicovich-Wilson, F. Pascale, B. Civalleri, K. Doll, N. Harrison, I. Bush, *et al.*, Crystal14 user's manual; university of torino: Torino, italy, 2014.

[19] For program description, see http://www.crystal.unito.it/.

[20] S. Moser, An experimentalist's guide to the matrix element in angle resolved photoemission, Journal of Electron Spectroscopy and Related Phenomena **214**, 29 (2017).

[21] E. L. Shirley, L. J. Terminello, A. Santoni, and F. J. Himpsel, Brillouin-zone-selection effects in graphite photoelectron angular distributions, Phys. Rev. B **51**, 13614 (1995).

[22] M. Mucha-Kruczynski, O. Tsyplyatyev, A. Grishin, E. McCann, V. I. Fal'ko, A. Bostwick, and E. Rotenberg, Characterization of graphene through anisotropy of constant-energy maps in angle-resolved photoemission, Physical Review B **77**, 195403 (2008).

[23] I. Gierz, J. C. Petersen, M. Mitrano, C. Cacho, I. C. E. Turcu, E. Springate, A. Stöhr, A. Köhler, U. Starke, and A. Cavalleri, Snapshots of non-equilibrium Dirac carrier distributions in graphene, Nature Materials **12**, 1119 (2013).

[24] J. C. Johannsen, S. Ulstrup, F. Cilento, A. Crepaldi, M. Zacchigna, C. Cacho, I. C. E. Turcu, E. Springate, F. Fromm, C. Raidel, T. Seyller, F. Parmigiani, M. Grioni, and P. Hofmann, Direct view of hot carrier dynamics in graphene, Phys. Rev. Lett. **111**, 027403 (2013).

[25] J. C. Johannsen, S. Ulstrup, A. Crepaldi, F. Cilento, M. Zacchigna, J. A. Miwa, C. Cacho, R. T. Chapman, E. Springate, F. Fromm, C. Raidel, T. Seyller, P. D. King, F. Parmigiani, M. Grioni, and P. Hofmann, Tunable carrier multiplication and cooling in graphene, Nano Letters **15**, 326 (2015).

[26] S. Aeschlimann, R. Krause, M. Chávez-Cervantes, H. Bromberger, R. Jago, E. Malić, A. Al-Temimy, C. Coletti, A. Cavalleri, and I. Gierz, Ultrafast momentum imaging of pseudospin-flip excitations in graphene, Physical Review B **96** (2017).

[27] G. Rohde, A. Stange, A. Müller, M. Behrendt, L.-P. Oloff, K. Hanff, T. Albert, P. Hein, K. Rossnagel, and M. Bauer, Ultrafast formation of a Fermi-Dirac distributed electron gas, Physical Review Letters **121** (2018).

[28] For program description, see https://www.bnl.gov/cmpmsd/flapwmbpt/.

[29] J. P. Perdew, K. Burke, and M. Ernzerhof, Generalized gradient approximation made simple, Physical Review Letters **77**, 3865 (1996).